# Effect of Welding Conditions on Microstructure and Properties of Type 316L Stainless Steel Submerged Arc Cladding

*Mathematical models were developed to predict process parameters needed to obtain the required dilution and hardness level*

BY N. MURUGAN AND R. S. PARMAR

ABSTRACT. Mathematical models were developed using response surface methodology for studying the direct and interaction effects of submerged arc welding parameters on stainless steel cladding geometry. The process parameters obtained from those models were employed to clad IS:2062 structural steel plate of 20-mm thickness using 316L stainless steel wire of 3.15-mm diameter. A low dilution of 22.57% was achieved in the cladding. Dilution was low when both voltage and welding speed were either high or low. Requirements of carbon and ferrite contents in the cladding were met by achieving low dilution in a single layer as well as multilayer cladding.

Color metallographic techniques revealed that in the as-welded condition of cladding, the microstructural constituents of the HAZ, fusion boundary zone, and cladding surfaced with a low dilution condition were bainite and ferrite, martensite, and austenite plus ferrite, respectively. The hardness of the existing martensitic structures at the intermediate mixed zones in overlays was below 400 VHN, which was attributed to the lower carbon content in the cladding. The solidification modes were found to be austenitic, ferritic, and austenitic and ferritic. The microstructure was found to be mainly cellular or cellular dendritic. The measured ferrite contents of cladding were well within their corresponding predicted values. The cladding possessed good ductility and resistance to intergranular corrosion.

*N. MURUGAN is Selection Grade Lecturer, Mech. Eng. Dept., C.I.T., Coimbatore, Tamil Nadu, India. R. S. PARMAR is Prof. of Mech. Eng., I.I.T., New Delhi, India.*

## Introduction

The automatic submerged arc welding (SAW) process has been shown to offer significant advantages to the fabrication industry for surfacing applications since its introduction. As success of weld cladding, especially stainless steel cladding, was proved, the use was expanded to larger and larger areas with the development of new techniques and processes such as addition of cold or hot filler metal wires, multiple wires, oscillating welding heads, single or multiple strips and addition of metal powders. The internal surfaces of paper digesters, urea reactors, atomic reactor containment vessels and pressurizers, hydrocrackers, to name some of the more spectacular examples, are often clad by welding to produce such a corrosion-resistant surface (Ref. 1).

Submerged arc strip cladding is a popular method employed for surfacing the inside of thick pressure vessels (Ref. 2). However, the process cannot be used for cladding all sizes and shapes because of the width of the electrode and the size of the molten pool. Since discontinuities, such as slag inclusions, sporadic undercutting and incomplete fusion, occur more frequently as electrode width increases, the use of an electrode more than 75 mm wide is difficult in conventional strip SAW practice (Ref. 3). Also, welding must be done in the flat position (1G). Often single wire submerged arc cladding is considered as a cost-effective technique to cladding smaller areas.

In cladding by a welding process, the most important aspect is the dilution of the filler metal with the base metal due to the arc penetration. Dilution reduces the alloying elements and increases the carbon content in the clad layer, which leads to a decrease in the corrosion resistance properties, percentages of delta ferrite content and other metallurgical problems (Refs. 4, 5). Also, control of dilution plays an important role in the economics of weld cladding processes because the economics of stainless steel cladding is dependent on achieving the specific chemistry at the practical deposition rate in a minimum number of layers. Although each process has an expected dilution factor, it is essential to establish a cladding procedure that will reduce its effects, consistent with good fusion and a sound deposit.

Also, with the increase in mechanization and automation in arc welding and cladding, the selection of welding procedures must be more specific to ensure that adequate weld bead quality is obtained (Ref. 6). Further, for the effective use of automated welding processes, it is

KEY WORDS

Stainless Steel Cladding
Surfacing
Mathematical Modeling
Bead Geometry
Microstructure
Microhardness
Modes of Solidificaiton
Delta Ferrite
Corrosion Resistance
EPR Technique

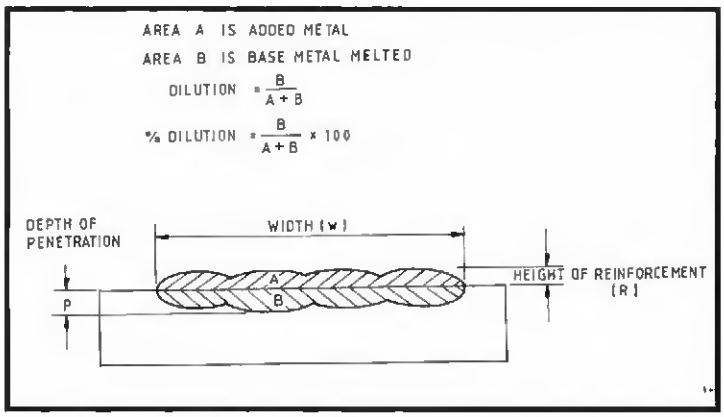


*Fig. 1 — Weld bead geometry.*

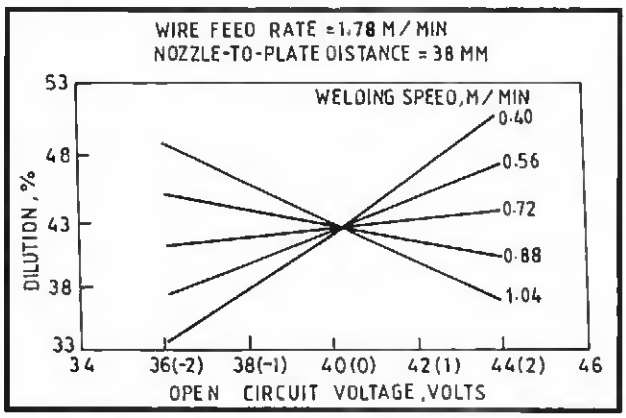


*Fig. 2 — Interaction effect of voltage and welding speed on dilution.*

essential that a high degree of confidence be achieved in predicting the weld bead geometry (Refs. 7, 8) to attain the desired mechanical and corrosion-resistant properties because the bead profile determines the amount of dilution involved. These requirements necessitate the development of mathematical models or equations relating to the weld bead dimensions (Fig.1) and the important controllable process parameters affecting the bead dimensions for establishing a cladding procedure. Hence, investigations were carried out to model an automatic single wire submerged arc cladding process that would have effective control of dilution to achieve necessary corrosion resistance and the mechanical properties in the deposited cladding. This paper deals with the effective use of such developed models for surfacing at a lower dilution condition. The analysis and selection of process parameters affecting bead geometry, especially dilution, using response surface methodology is presented. The quality of the stainless steel claddings surfaced at lower dilution conditions has been evaluated with the help of metallurgical studies, bend, and corrosion tests.

## Development of Mathematical Models

Mathematical models were developed by carrying out the following steps:

1) The important independent process control variables were identified.

2) The upper and lower limits of the control variables were found, *viz.*, open circuit voltage (V), wire feed rate (F), welding speed (S) and nozzle-to-workpiece distance (N).

3) The design matrix was developed.

4) The experiments were conducted per the design matrix.

5) The responses were recorded, *viz.*, penetration (P), weld width (W), reinforcement (R), and dilution (D).

6) Second order polynomial equation was selected.

7) The coefficients of the polynomials were calculated.

8) The adequacy of the models developed were checked.

9) The significance of the regression coefficients were tested and the mathematical models were finalized.

The above steps were well detailed in Ref. 9. The levels of process parameters selected for investigation, with their units and notations, are given in Table 1. As both arc voltage and welding current could not be controlled directly and they are interdependent, they were not considered as factors. But welding current depends on wire feed rate; which is directly controllable, wire feed rate was taken as a factor instead of welding current. Open circuit voltage was used as a parameter instead of arc voltage because it was noticed during the investigation that the arc voltage increased proportionately (not linearly) when open circuit voltage was increased, while the values of wire feed rate, welding speed and nozzle-to-workpiece distance were kept constant. For example, the arc voltage increased from 26 to 34 V when open circuit voltage was changed from 36 to 44 V and wire feed rate, welding speed and nozzle-to-workpiece distance were kept constant at 1.78 m/min, 0.72 m/min and 38 mm, respectively.

The final mathematical expressions relating the various process parameters to the weld bead geometry shown in Fig. 1 are presented below (all welding variables are to be used in coded form).

$$P = 2.763 + 0.454\,F - 0.296\,S - 0.131\,N - 0.124\,FS \quad (1)$$

$$R = 2.681 - 0.138\,V + 0.242\,F - 0.319\,S + 0.097\,VS + 0.147\,S^2 \quad (2)$$

$$W = 37.863 - 1.933\,V + 0.775\,F - 4.542\,S - 0.827\,F^2 \quad (3)$$

$$D = 42.552 + 0.667\,V + 2.358\,F + 0.197\,S - 1.062\,N - 1.83\,VS \quad (4)$$

Where

P = Depth of penetration, mm
R = Height of reinforcement, mm
W = Weld width, mm
D = Dilution, %
V = Arc voltage
F = Wire feed rate
S = Welding speed
N = Nozzle-to-workpiece distance

The above equations with the control variables and response parameters in their commonly used units are given below.

$$P = -1.593 + 3.894\,F + 3.461\,S - 0.033\,N - 2.985\,FS \quad (5)$$

$$R = 16.907 - 0.287\,V + 0.929\,F - 22.373\,S + 0.303\,VS + 5.744\,S^2 \quad (6)$$

$$W = -24.452 + 0.967\,V + 46.555\,F - 28.385\,S - 12.24\,F^2 \quad (7)$$

$$D = -142.422 + 4.451\,V + 9.071\,F + 229.984\,S - 0.266\,N - 5.719\,VS \quad (8)$$

**Table 1 — Control Parameters and Their Levels of Submerged Arc Surfacing**

| Parameter | Units | Notation | Factor Levels −2 | −1 | 0 | 1 | 2 |
|---|---|---|---|---|---|---|---|
| Open Circuit Voltage | Volt | V | 36 | 38 | 40 | 42 | 44 |
| Wire Feed Rate | m/min | F | 1.26 | 1.52 | 1.78 | 2.04 | 2.3 |
| Welding Speed | m/min | S | 0.40 | 0.56 | 0.72 | 0.88 | 1.04 |
| Nozzle-to-workpiece Distance | mm | N | 30 | 34 | 38 | 42 | 46 |

The units of P, R ,W are mm, and that of D, V, F, S, and N are %, volts, m/min, m/min, and mm, respectively.

For the ease of computation and representation of data in graphical form the equations with parameters in their coded forms were used.

## Analysis of Developed Mathematical Models

The direct and the interaction effects of process parameters on bead geometry have been well presented in Refs. 9 and 10. The interaction effects of open circuit voltage and welding speed on dilution are given below.

### Interaction of Open Circuit Voltage and Welding Speed on Dilution

It is evident from Figs. 2 and 3 that dilution (D) increases with an increase in open circuit voltage (V) when welding speed (S) is low. This is due to the more heat input per unit length of weld as S is low, resulting in more melting of base metal and a high D. A larger and wider bead with less reinforcement results when V increases, while S is kept at its low level. The weld bead becomes narrow and thin when S increases due to lesser amount of filler metal deposited. Also, when S is high, less amount of base metal is melted, resulting in lower D. Due to this, D decreases even when V is increased while S is high. This is clearly shown in the contour graph of Fig. 3. Dilution was lower when voltage was at –2 level and S was at –2 level and when V was +2 and S was +2 level. As the range of speed taken for investigation was large when compared to that used for V, at higher welding speed the increase in V did not influence D much.

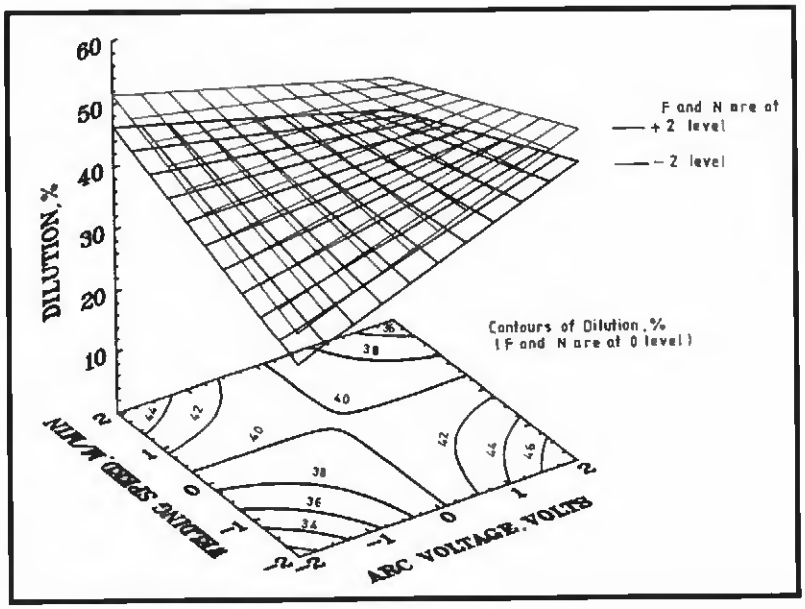


*Fig. 3 — Perspective surface and contouring of dilution model.*

It is seen from the response surfaces that the minimum dilution of 30.32% was achieved, when V and S were at –2 level, which is clearly depicted by the lowest point on the response surface by the left-hand lower corner of Fig. 3. From Equation 4, a lower D of 26.664% could be obtained when voltage, speed and wire feed rate are kept at their low levels (–2) and NPD at its high level (2).

To achieve dilution below 25%, an electrode-to-work angle of 45 deg was employed after conducting trial runs to study its effect on dilution. It is apparent from Fig. 4 that dilution decreases with the decrease in electrode-to-work angle or travel angle when voltage, speed and

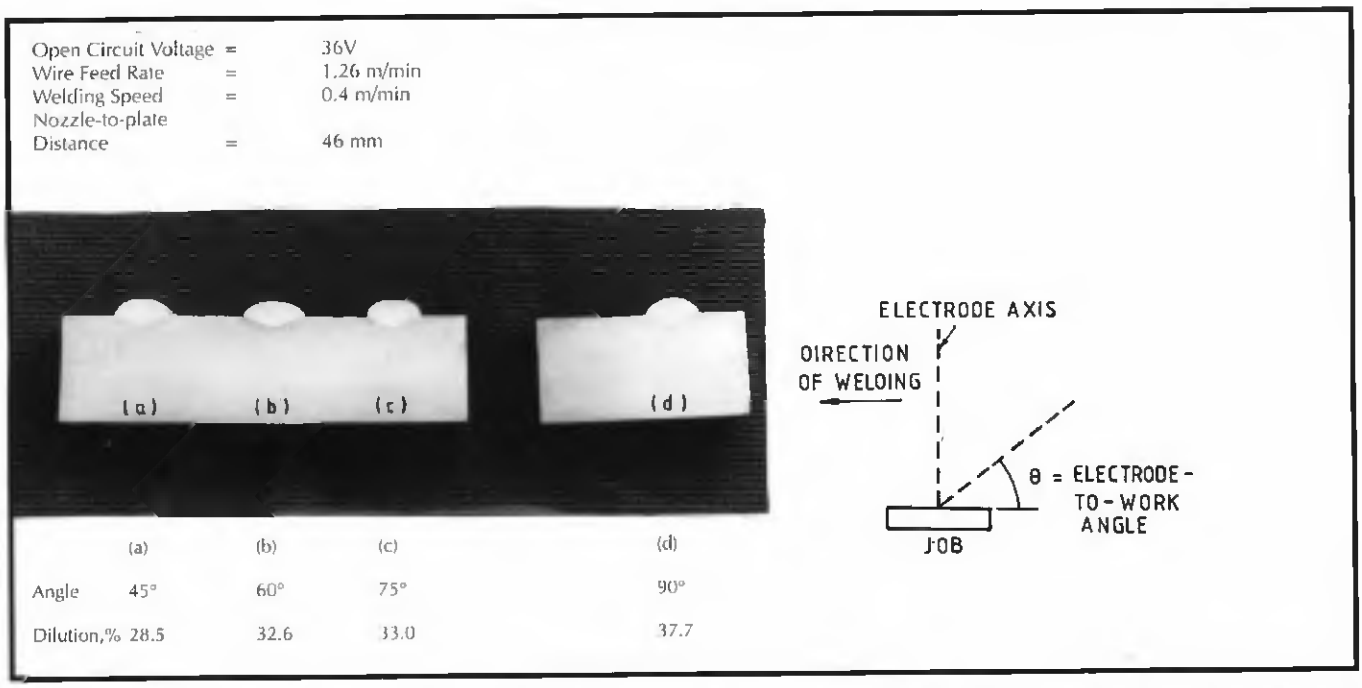


*Fig. 4 — Effect of electrode-to-work angle on dilution. A — 45-deg angle, 28.5% dilution; B — 60-deg angle, 32.6% dilution; C — 75-deg angle, 33% dilution; 90-deg angle, 37.7% dilution.*

*Fig. 5 — Bead configuration of submerged arc cladded specimen surfaced at lower dilution condition.*

*Fig. 6 — Cross section of typical cladded side bend test specimens showing penetration profile.*

wire feed rate are kept at their low levels and NPD at its high level.

## Experimental Investigations

### Surfacing at Lower Dilution Conditions

Submerged arc surfacing of structural steel IS:2062 plates of 20 mm thickness was carried out using the process parameters given in Table 2. The chemical compositions of base and filler metals are given in Table 3. Four beads, each 150 mm long, were laid using 316L stainless steel wire of 3.15 mm diameter with a 40% overlap of beads. Positive electrode polarity was used. The interpass temperature was maintained at 150°C. The surfaced plate was cross-sectioned at its midpoint to obtain test specimens of 10 mm width. These specimens were further prepared by usual metallurgical polishing methods and etched with 2% nital. The weld-bead profiles were traced using an optical profile projector and the bead dimensions, *viz.*, penetration (P), reinforcement (R), and width (W) were measured. With the help of a planimeter, the areas of the base plate melted and the weld metal forming the reinforcement were measured and the percentage dilution was found to be 22.57%. The corresponding bead configuration of a typical specimen is shown in Fig. 5. This specimen prepared from the single layer cladding was coded as T1 for identification.

An area of about 100 x 150 mm was surfaced using the same process conditions as mentioned above. Specimens for bend testing were prepared by cutting them perpendicular to the welding direction at three locations, one at its middle and two specimens each at 15 mm from their respective ends, to have a 12 mm width. Two sides of all three specimens were ground to the final size of 150 x 23 x 10 mm. Figure 6 depicts the penetration profiles of a typical sample prepared for side bend testing.

### Multilayer Surfacing

It is a common practice to deposit two or more layers of cladding to satisfy the required thickness and chemistry of the deposit (Refs. 1, 11). This is obviously carried out to nullify the effect of dilution at the first layer and especially to fulfil, the requirement of carbon level in the deposit. Using the same process parameters with their corresponding predicted values, multilayer surfacing was carried out with 316L stainless steel wire of 3.15-mm diameter, and they were identified by their corresponding coded numbers for further analysis: 1) single layer of 316L wire of 3.15-mm diameter (T1); 2) two layers of 316L wire of 3.15-mm diameter (T2); and 3) three layers of 316L wire of 3.15-mm diameter (T3).

In two-layer surfacing, the first layer was deposited with six passes employing the welding conditions mentioned above and the second layer was deposited onto the first layer with four passes using the same welding conditions. In surfacing three layers, the first layer was deposited with eight passes employing the same welding conditions that were used for single layer as well as for double layer cladding followed by depositing a second layer onto the first layer with six passes. The third layer was deposited onto the second layer with four passes.

Specimens of a size 20 x 20 x 10 mm prepared from top surfaces of claddings (T1, T2 and T3) were used for the sensitization test. Two test specimens from each cladding were prepared and used for this EPR test. The following experimental procedure was employed for the preparation of specimen surface for corrosion experiments: The surface was prepared within one hour of the experiment and was stored in a suitable desiccating cabinet. Wet grinding with 240 grit and 400 grit SiC paper was carried out, followed by wet polishing with 600 grit SiC paper until previous coarse scratches

**Table 2 — SAW Process Parameters Employed for Cladding**

| Sample No. | Process Parameter | Setting |
|---|---|---|
| 1 | Open circuit voltage | 36 V |
| 2 | Arc voltage | 25 V |
| 3 | Welding current | 225 A |
| 4 | Welding speed | 0.4 m/min |
| 5 | Nozzle-to-workpiece distance | 46 mm |
| 6 | Shielding medium | Automelt SS Flux Grade I |
| 7 | Wire diameter | 3.15 mm |
| 8 | Electrode polarity | Positive |

**Table 3 — Chemical Composition of Base and Filler Metals**

| Sample No. | Material | Elements, % C | Si | Mn | Cr | Ni | Mo | Cu | S | P |
|---|---|---|---|---|---|---|---|---|---|---|
| 1 | Base metal | 0.250 | — | 1.60 | — | — | — | — | 0.055 | 0.055 |
| 2 | 316L wire 3.15-mm dia | 0.018 | 0.42 | 1.62 | 19.26 | 12.42 | 2.30 | 0.140 | 0.040 | 0.017 |

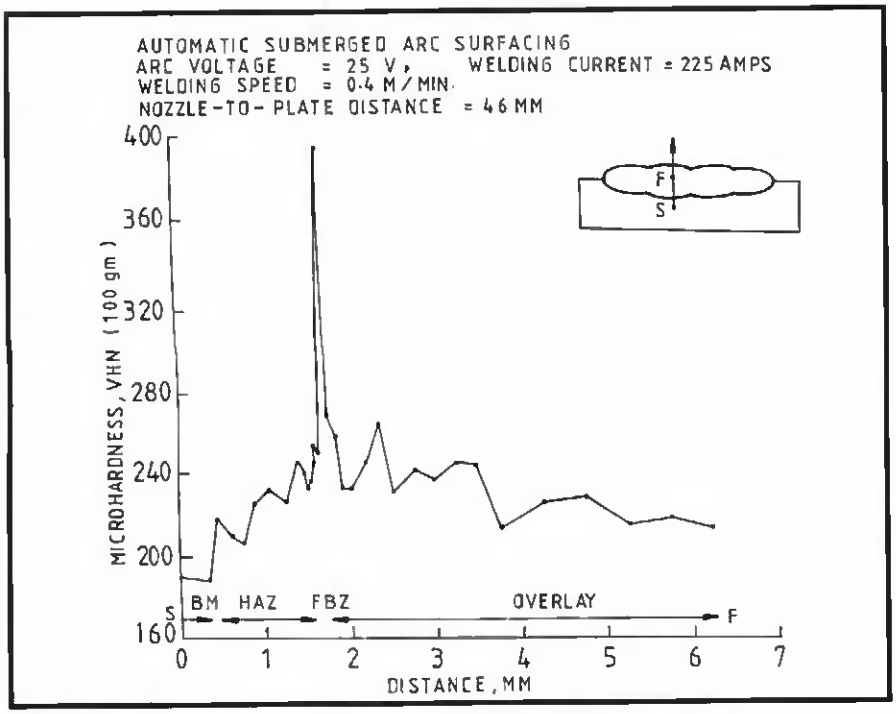


*Fig. 7 — Microhardness distribution in single-layer 316L cladding (T1).*

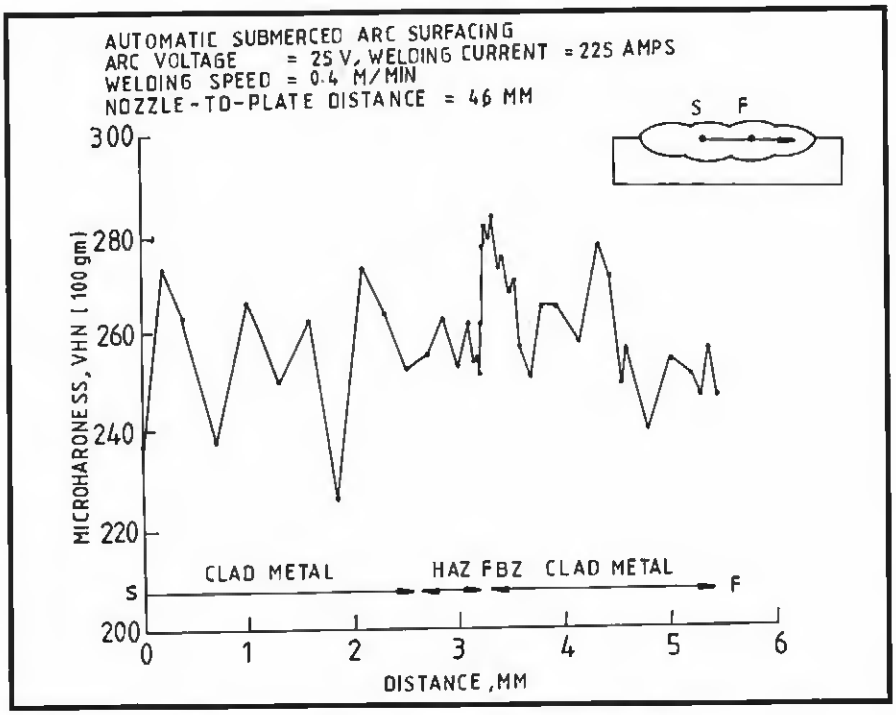


*Fig. 8 — Microhardness distribution in single-layer 316L cladding (T1).*

**Table 4 — Chemical Compositions of Stainless Steel Cladding**

| Sample No. | Material | C | Si | Mn | Cr | Ni | Mo | Cu | Nb | Ti |
|---|---|---|---|---|---|---|---|---|---|---|
| | | Elements, % | | | | | | | | |
| T1 | 316L | 0.055 | 0.663 | 1.181 | 14.900 | 9.560 | 1.923 | 0.106 | 0.007 | 0.002 |
| T2 | 316L | 0.026 | 0.762 | 1.249 | 18.389 | 11.478 | 2.341 | 0.147 | 0.014 | 0.004 |
| T3 | 316L | 0.021 | 0.751 | 1.375 | 18.946 | 11.965 | 2.379 | 0.129 | 0.100 | 0.002 |

were removed, rinsed with water, and dried. The specimens were finally polished in two additional stages with 6 and 1 μm diamond paste or 0.05 μm alumina slurry on a nylon or silk cloth over microcloth prepared polishing wheel as per ASTM E3.

**Metallurgical Studies**

The experimental details of the various aspects of the metallurgical studies undertaken are furnished under respective headings below. A set of samples in as-welded conditions taken from the cladded plates surfaced at lower dilution conditions, including the multilayer claddings described previously, were utilized for these studies. Standard metallurgical procedures were used to prepare the samples for microhardness survey and microstructural studies. The cross sections of specimens parallel and perpendicular to welding directions and their top surfaces were polished. Sample code numbers were used to identify the corresponding samples.

*Analysis of cladding chemistry*: The chemical composition of the samples mentioned above were analyzed using the Spectrovac System based on the atomic emission analytical technique. The top surfaces of the samples were ground flat for a 2-mm depth and three test burns were taken to find out the chemical composition of the important elements present in the cladding. The average of the three readings were calculated and tabulated for various elements as shown in Table 4. Using these values the potential factors or equivalents of Schaeffler, Delong, and WRC-1992 constitutional diagrams were calculated and tabulated as shown in Table 5. An analysis of nitrogen was not possible, and it was taken as 0.06% for the SAW process (Refs. 11, 12).

*Microhardness survey*: Standard metallurgical procedures were used to prepare the samples for microhardness studies and the samples were etched suitably to facilitate a microhardness survey along the different metallurgical zones of the cladding such as unaffected base metal, HAZ, transition zone and clad metal. The etchant used to reveal base metal and HAZ was 2% nital. The color etchant used to reveal the clad microstructure was 20 g ammonium biflouride and 0.5 g of potassium metabisulfite in 100 mL of distilled water, and the etching time was 2–4 min at 40°C (Refs. 13, 14).

The Wolpert microhardness tester was employed to carry out microhardness surveys on various parts of the as-

welded specimens, which were cut perpendicular to the welding direction, starting from the heat-unaffected base metal up to the weld metal farthest from the weld interface along the centerline of a single bead as well as across two adjacent beads. A Vickers indenter with 100-g load was used to make indentations on all specimens. The microhardness values obtained were plotted against the distance covered along its different zones in graphical form for quick analysis and a few of them are given in Figs. 7–9.

*Ferrite measurement*: The top surfaces of all specimens obtained from the surfaced plates were ground flat to facilitate the measurement of ferrite content of the clad in the as-welded condition. The delta ferrite contents were measured based on magnetic method using the ferritescope manufactured by Fischer Instrumentation (GB) Ltd. Six readings were taken on the top of specimens in transverse and longitudinal directions and the average values of ferrite content were tabulated as shown in Table 6. The values of WRC ferrite number corresponding to the measured ferrite content were found by linear interpolation from Delong diagram (Ref. 15) and are given in Table 6. The ferrite content was also estimated using Schaeffler, Delong, and WRC-92 constitutional diagrams, which relate the alloy chemistry to the volume fraction of ferrite present (% ferrite) or ferrite number (FN) in austenitic steels and Seferian equation (Refs. 16, 17) based on Schaeffler equivalents depicted in Table 5, and were tabulated as shown in Table 6 to compare the estimated and the predicted values of ferrite content.

*Microstructural studies*: Standard metallurgical procedures were employed to prepare all the samples taken for this study, and color metallography was used to reveal various phases present in all zones of the claddings. Since color etching makes both primary and secondary structures visible (Ref. 18) due to the reaction between etching compound and crystal segregations of primary solidified crystals, it was especially employed for stainless steel weld metal to assess the modes of solidification because solidification cracking in a stainless steel is related to the solidification mode rather than only its ferrite content at room temperature (Ref. 19). The same etchants used to reveal microstructures for carrying out microhardness survey were also employed for preparing samples for microstructural studies.

The etched samples were subjected to an extensive microstructure survey using a Vickers M-17 optical microscope to study the microstructure in the base metal, HAZ, weld interface and clad

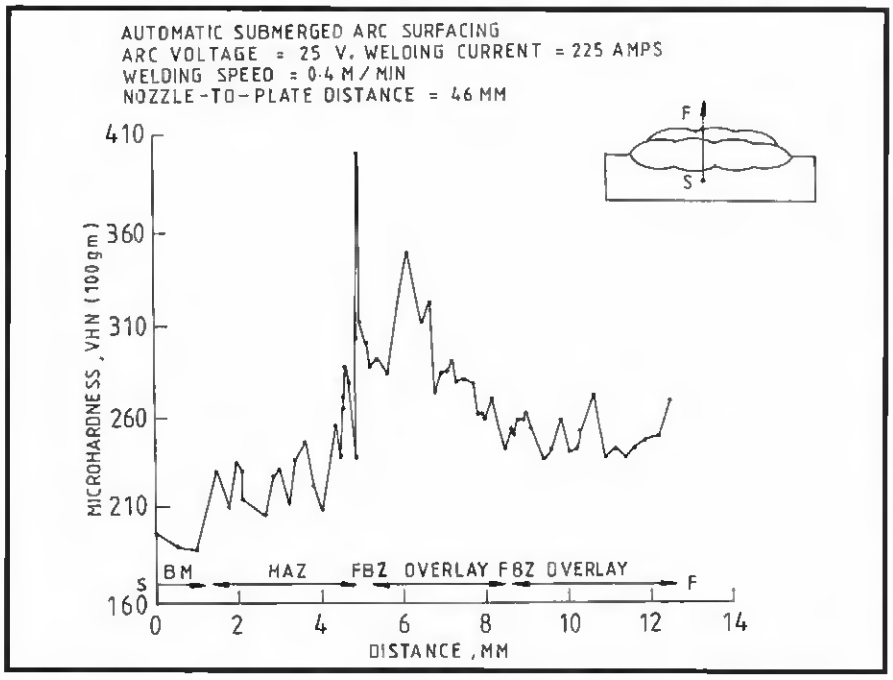


*Fig. 9 — Microhardness distribution in multilayer 316L cladding (T2).*

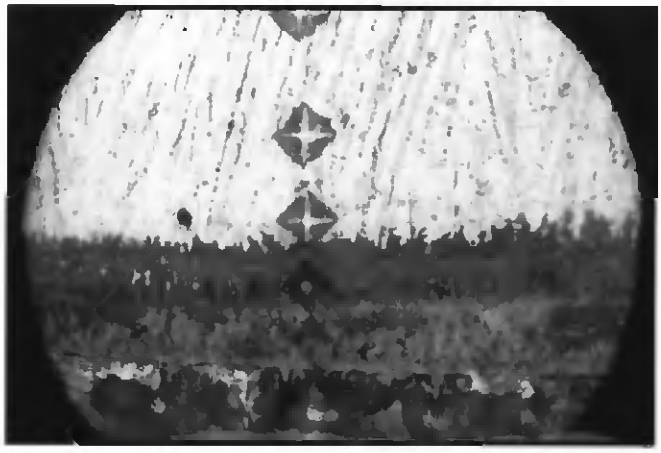

*Fig. 10 — Microstructure at the base metal-clad metal interface showing a typical "beach" IMZ. The maximum hardness of the IMZ was 330.1 VHN (100 g). T1: A — 1600X; B — 4000X.*

**Table 5 — Chromium and Nickel Equivalents of Claddings**

| Sample No. | Sample Code No. | Potential Factors (%) SCE | SNE | DCE | DNE | HCE | HNE | WCE | WNE |
|---|---|---|---|---|---|---|---|---|---|
| 1 | T1 | 17.8 | 11.8 | 17.8 | 13.6 | 18.5 | 13.3 | 16.8 | 12.7 |
| 2 | T2 | 21.9 | 12.9 | 21.9 | 15.3 | 22.8 | 15.0 | 20.7 | 14.0 |
| 3 | T3 | 22.5 | 13.3 | 22.5 | 15.1 | 23.5 | 15.2 | 21.4 | 13.9 |

SCE = Schaeffler chromium equivalent
%Cr + %Mo + 1.5% Si + 0.5% Nb.
SNE = Schaeffler nickel equivalent
%Ni + 30% C + 0.5% Mn.
DCE = Delong chromium equivalent
%Cr + %Mo + 1.5% Si + 0.5% Nb.
DNE = Delong nickel equivalent
%Ni + 30% C + 30% N + 0.5% Mn.
HCE = Hammer and Svensson chromium equivalent
%Cr + 1.37% Mo + 1.5% Si + 2% Nb +3% Ti.
HNE = Hammer and Svensson nickel equivalent
%Ni + 22% C +14.2% N + 1.31% Mn + %Cu.
WCE = WRC-1992 diagram chromium equivalent
%Cr + %Mo + 0.7% Nb.
DNE = WRC-1992 diagram nickel equivalent
%Ni + 35% C +20% N + 0.25% Cu.

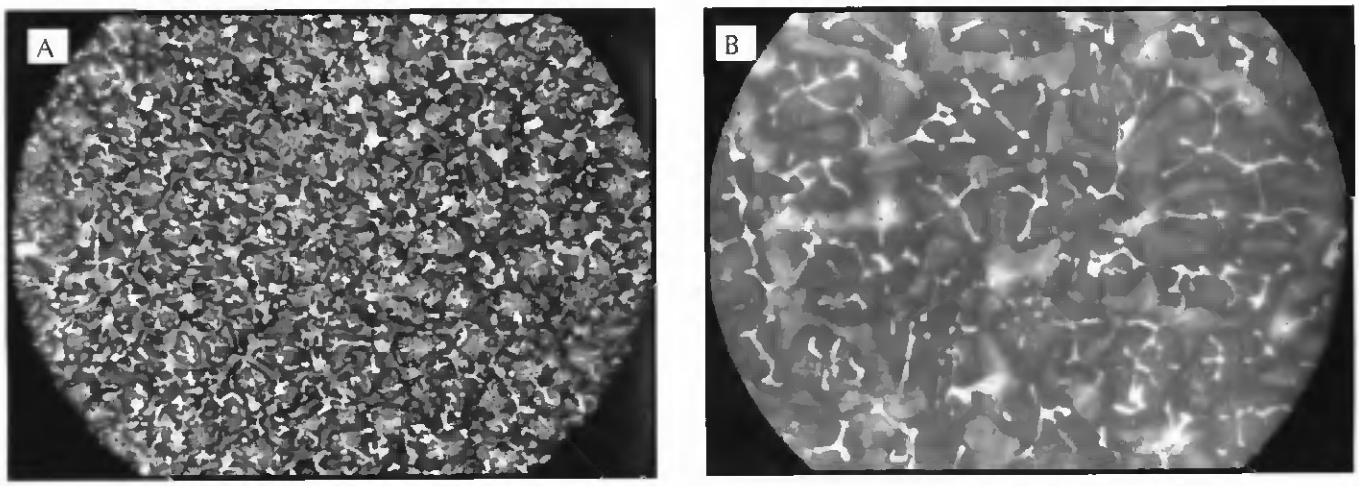


*Fig. 11 — Microstructure showing primary ferritic mode (FA) of solidification with vermicular morphology. T1: A — 1600X; B — 4000X.*

metal under different magnifications ranging from 100X to 1000X. A large number of zones of interest were photographed to study the extent of coalescence as well as the type and nature of microstructure present. These photomicrographs were enlarged while taking the reprints, and the actual magnification obtained is indicated with each figure. Some typical photomicrographs have been presented in Figs. 10–15.

**Table 6 — Comparison of Predicted and Measured Ferrite Content of Stainless Steel Claddings**

| Sample No. | Sample Code No. | SDF % | Predicted Ferrite Content DDF % | DDF FN | WDF FN | SEF % | Measured Ferrite content % | FN |
|---|---|---|---|---|---|---|---|---|
| 1 | T1 | 0.0 | 0.0 | 0.0 | — | 0.4 | 3.7 | 3.7 |
| 2 | T2 | 7.5 | 7.3 | 7.7 | 5.3 | 9.6 | 9.3 | 10.2 |
| 3 | T3 | 9.5 | 9.5 | 10.5 | 7.9 | 10.3 | 11.0 | 12.4 |

SDF = Predicted ferrite from Schaeffler Diagram.
DDF = Predicted ferrite from Delong Diagram.
WDF = Predicted ferrite from WRC-1992 Diagram.
SEF = Predicted ferrite from Seferian Equation (Ref. 16).
3 (Crequ. – 0.93 Nicqu. – 6.7), where Crequ. and Nequ. are defined by Schaeffler.

**Table 7 — EPR Test Conditions**

| Sample No. | Description | Single-Loop Test | Double-Loop Test |
|---|---|---|---|
| 1 | Scan rate | 1.667 mV/s | 1.667 mV/s |
| 2 | Scan increment | 0.500 mV | 1.000 mV |
| 3 | Initial potential | 0.200 V | –0.400 V |
| 4 | Passivation potential | 0.200 V | – |
| 5 | Passivation time | 2 min. | – |
| 6 | Final potential | –0.500 V | –0.400 V |
| 7 | Current range | Auto | Auto |
| 8 | Step time | 0.3 s | 0.6 s |
| 9 | Line Synchronization | No | No |
| 10 | Rise time | High stability | High stability |
| 11 | Working electrode | Solid | Solid |
| 12 | Sample area | 1.000 $cm^2$ | 1.000 $cm^2$ |
| 13 | Reference electrode | AgCl, 0.197 V | AgCl, 0.197 V |
| 14 | Vertical potential (Potential at which scan was reversed) | – | 0.300 V |
| 15 | Threshold current density | – | 0.1μA/$cm^2$ |

**Evaluation of Cladding Ductility and Corrosion Resistance**

Three specimens were prepared from the plate surfaced at lower dilution conditions to evaluate the influence of welding parameters and welding conditions on plastic properties of weld deposit. The quality of joining between the clad layer and base metal, and corrosion resistance were also evaluated. Guided side bend tests were carried out using a standard bend testing jig. Specimens were bent through 180 deg.

The resistance to intergranular corrosion (IGC) or sensitization of the cladding was tested by the electrochemical potentiokinetic reactivation (EPR) technique (Ref. 20) using single- and double-loop methods. The test conditions of single and double-loop EPR tests are given in Table 7. Potentiokinetic curves have been drawn for single- and double-loop EPR methods to assess the sensitization behavior of stainless steel cladding. A few EPR curves are shown in Figs. 16–19.

## Results and Discussion

Results obtained by the aforementioned experimental investigations are presented and discussed in the same sequence as detailed in the previous section.

**Bead Characteristics**

The surfaced beads were smooth and shiny with fine ripples. The slag was easily detachable causing no impression on the surface. Extensive macroscopic examination of surfaces and many cross sections revealed that the deposited cladding was sound and free from discontinuities such as porosity, slag inclusion, and cracks. The calculated dilution in single-layer surfacing was 22.57%.

**Analysis of Chemistry of Claddings**

It is evident from Table 4 that the chemical composition of cladding depends on the amount of dilution caused by the intermixing of base metal and the filler metal, and alloy content of clad metal increased from the first layer to second layer (samples T1 and T2). The com-

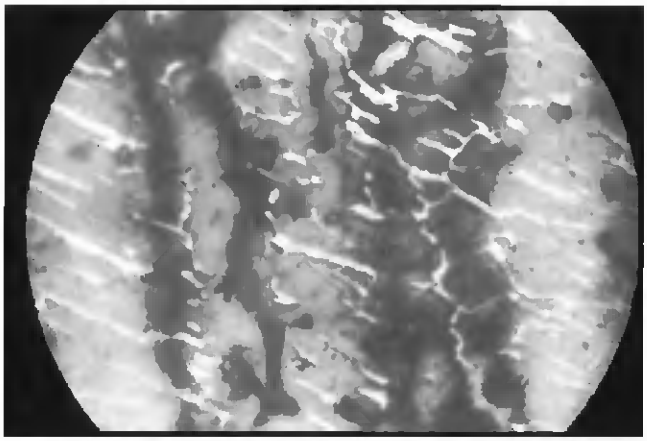

*Fig. 12 — Microstructure of second layer of 316L cladding showing primary ferritic mode with lathy ferrite morphology (T3, 4000X).*

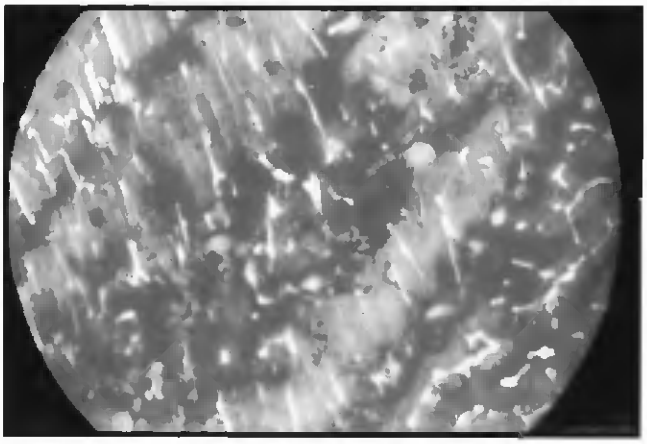

*Fig. 13 — Microstructure of first layer of 316L cladding showing primary ferritic mode with both vermicular and lathy ferrite morphology (T1, 4000X).*

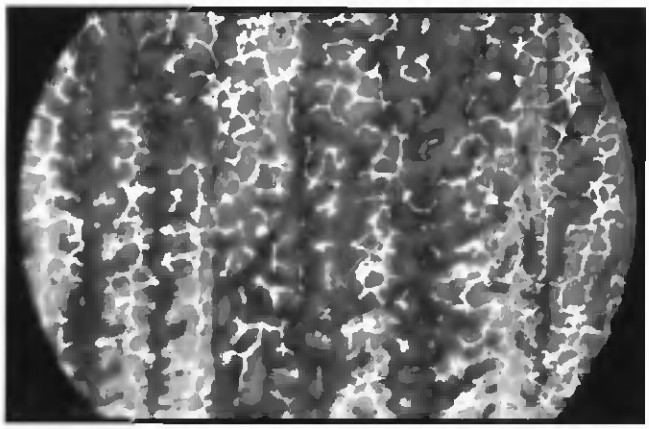

*Fig. 14 — Microstructure of third layer of 316L cladding showing primary ferritic mode with continuous and discontinuous vermicular ferrite morphology (T3, 1600X).*

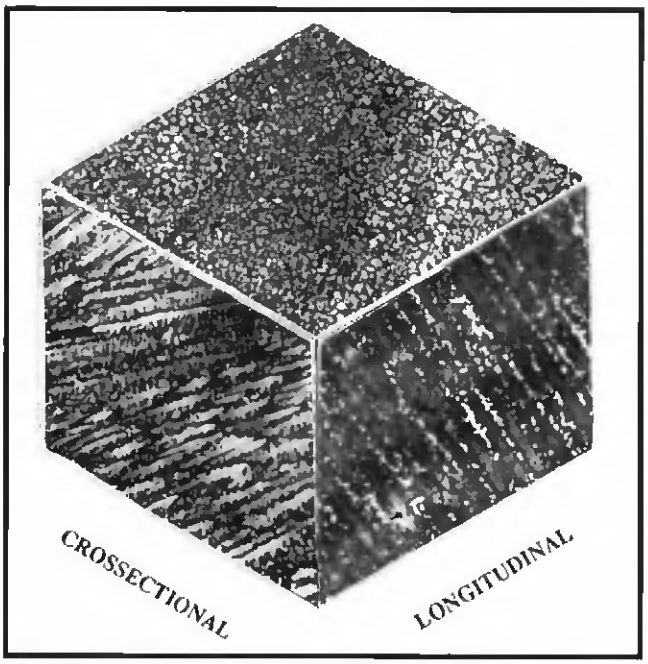


*Fig. 15 — Microstructures of single-layer 316L cladding viewed from three mutually perpendicular directions (T1, 400X).*

position of second and third cladding meets the required specification of ER316L stainless steel to satisfy the required corrosion resistance of the cladding. The carbon contents of the cladding were all well within the maximum limit of 0.03% except the first layer of cladding (T1). This was attributed to the fact that the dilution achieved in SAW was about 22%.

The various equivalents supplied in Table 5 were utilized to predict the ferrite content of the cladding, as well as the solidification mode that occurred in the cladding. These predicted values are listed respectively in Tables 6 and 8 for comparison with actual values and for further analysis.

#### Analysis of Microhardness Survey

The microhardness survey carried out in various zones of multipass stainless steel cladding along the centerline of single beads and across two adjacent beads and the same are presented in Figs. 7 to 9. A hardness curve may be divided into four parts such as unaffected base metal (BM), heat-affected zone (HAZ), fusion boundary zone (FBZ) and cladding or weld metal (WM).

It is evident from the figures that the microhardness values of HAZ, particularly the coarse-grained region of HAZ, were higher than the unaffected base metal. This may be due to the formation of bainitic structure in the HAZ. The hardness of the HAZ close to the fusion boundary zone was found to be less than the peak hardness values of the HAZ. This could possibly be due to the formation of coarse bainite in that zone of the HAZ.

In the third zone marked as FBZ, the hardness suddenly increases to a very high value and then drops abruptly to a low value. This increase in hardness was due to the presence of the martensite. Because of a composition gradient, the transition zone between austenitic cladding and base metal (carbon steel) is martensitic, whose hardness depends on the carbon content of the zone. The formation of martensite along the weld interface has been reported in the literature (Refs. 21, 22). In the as-welded condition, the carbon content in this martensitic zone was relatively low and the hardness was, therefore, low. The maximum hardness value of these zones was below 400 VHN. On entering the cladding region, the hardness decreased drastically from the peak value and then remained more or less the same in the remaining portion of the cladding.

From Fig. 8, it is apparent that the hardness value of the weld metal, as well as the reheated and remelted portions of weld metal due to multipass surfacing, was not appreciably altered. This could

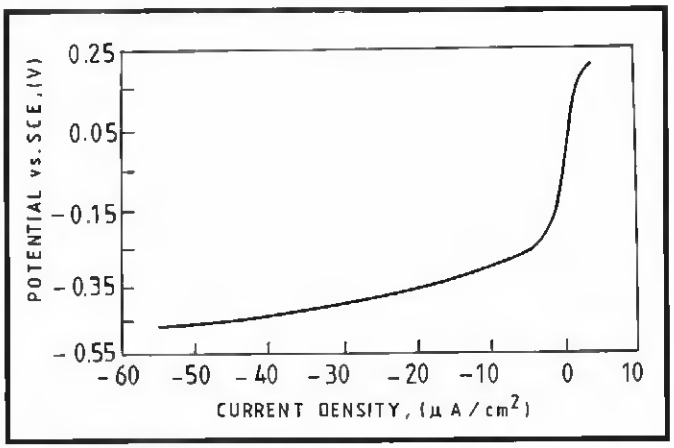


*Fig. 16 — Single-loop EPR curve for 316L multilayer cladding (T2).*

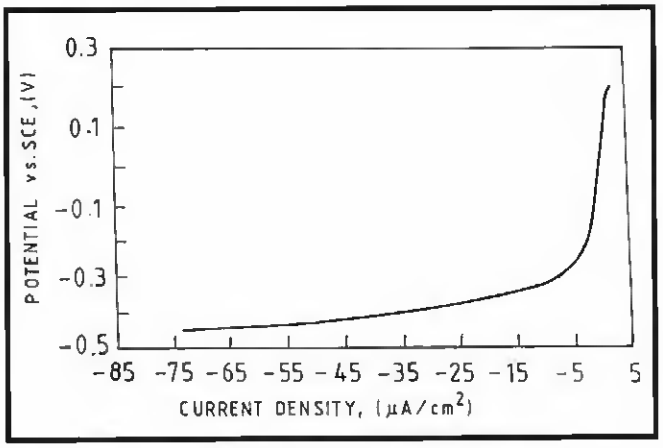


*Fig. 17 — Single-loop EPR curve for 316L multilayer cladding (T3).*

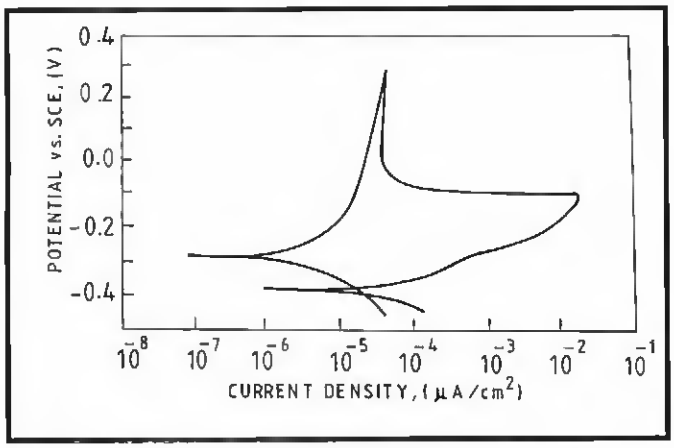


*Fig. 18 — Double-loop EPR curve for 316L single-layer cladding (T1).*

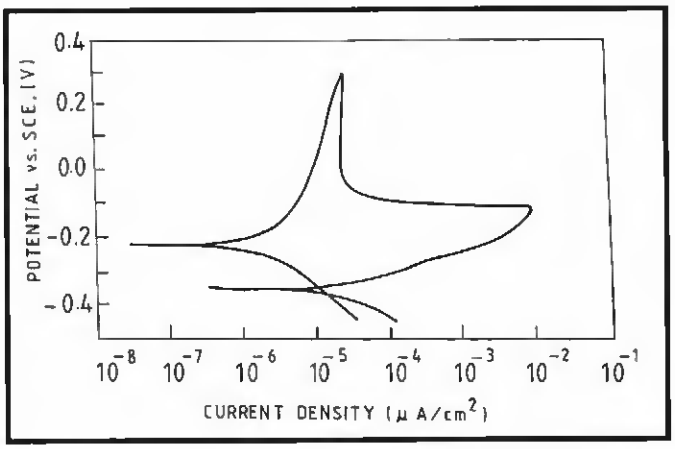


*Fig. 19 — Double-loop EPR curve for 316L multilayer cladding (T3).*

possibly be due to a lower welding speed employed for surfacing to obtain a lower dilution, which reduced the cooling rate. Also, Fig. 9 represents not only a multi-pass condition, but also a multi-layer condition, and in those claddings, the hardness of the first layer was more than that of the second layer of cladding. This may be due to the occurrence of higher dilution in the first layer than that of the second layer.

#### Analysis of Ferrite Content

It is an accepted practice to specify a minimum content of δ-ferrite in the austenitic cladding or weld metal to reduce hot cracking tendency. Again, depending upon the service conditions and considering the possibility of sigma phase formation, a maximum content of δ-ferrite is prescribed in different codes and specifications. The minimum recommended ferrite content for 316L stainless steel is 2% (Refs. 23, 24).

In the present study, five δ-ferrite estimation methods were employed, *viz.*, ferritescope based on magnetic method and Schaeffler, Delong, WRC-1992 constitutional diagrams and Seferian equation (Refs. 16, 17) based on chemical composition. All the results of delta ferrite estimations are provided in Table 6.

From Table 6, though all the above five methods described for evaluating δ-ferrite content did not yield similar results for all test samples, all values are very close to each other. It is to be noted that the prediction accuracy of the Schaeffler and Delong diagrams was 14% and 12%, respectively (Refs. 1,18) and the accuracy of WRC-1992 diagram was claimed to be higher than that of Delong diagram (Ref. 25).

#### Microstructural Analysis

Photomicrographs shown in Figs. 10–15 depict characteristic primary solidification structures as they appear in different zones of a weld bead of austenitic stainless steel cladding with normal cooling in air. The primary structures were made visible by the use of color etchants. The interior of the cell becomes blue colored, while the borders of the cell appear brown or yellowish. From the position of the ferrite in the interior or borders of the cells, it will be recognized that the weldment solidified as ferrite or austenite (Ref. 26). The solidification substructure was found to be mainly cellular or cellular dendritic. Narrow zones of planar growth were, however, found along the weld interface.

Figure 10 represents the solidification of single layer cladding (T1) near the weld interface at 1600X magnification along a section normal to the welding direction. The presence of "beach" structure (Ref. 27) is well depicted as a dark bluish-brown colored section. This structure, which is feathery along the weld interface, is martensitic and about 70 μm wide having the hardness value of 330.1 VHN (100-g load). Due to the low carbon content of the welding wire, the hardness was less. The hardness decreased from the weld interface to the cladding as seen from the indentation marks.

From Figs. 11–13, it is apparent that

weld metal solidified with two morphologies characterized by vermicular ferrite (Figs. 11, 13) and lathy ferrite (Figs. 12, 13) both located at cell axes. This was of ferritic-austenitic (FA) solidification mode often termed as primary ferrite solidification: the leading phase was the δ-ferrite and austenite solidified from the rest of the melt and also through a solid-state δ-γ transformation occurring at high temperature. The blue areas of the structure represent the already solidified cellular crystals consisting of primary delta ferrite. In between is the residual melt, which appears as a brownish tinted structural constituent. A bright structural constituent is also visible in the primary precipitated delta ferrite crystals. This represents the residual delta ferrite, which remains after δ-γ transformation and which is identified in conventional etching as delta ferrite (Refs. 18, 26). Both continuous and discontinuous vermicular ferrite morphologies are shown in Fig. 14 and the mode of solidification was FA. Figure 15 represents the microstructures observed at sections mutually perpendicular to each other in the single layer cladding (T1). According to the direction of growth of the cells and direction of sectioning, the cell colonies appear as stripes or dots (Ref. 26).

The microstructure of a stainless steel weld is dependent on both the solidification mode and δ-γ transformation on cooling. Kujanpää, *et al.* (Ref. 28) have reported that when the ratio of $Cr_{equ}/Ni_{equ}$ based on Schaeffler equivalent is < 1.48, austenitic and austenitic-ferritic solidification occurs and if the ratio is between 1.48 and 1.95, then ferritic solidification takes place. But Suutala (Ref. 29) has shown that the transition from primary austenitic to ferritic solidification in stainless steel welds occurs at a (Cr/Ni) equivalent ratio based on Hammer and Svensson equivalents of 1.55. From the calculated potential factors of cladding given in Table 5, the values of $Cr_{equ}/Ni_{equ}$ based on Schaeffler, and Hammer and Svensson equivalents were calculated, and the modes of solidification of the cladding were predicted based on these ratios of equivalents and also from the WRC 1992 constitutional diagram. These predicted modes of solidification and the observed modes of solidification were tabulated as shown in Table 8 for easy comparison. It is evident from the table that the predicted modes of solidification are well in agreement with the observed modes of solidification.

**Table 8 — Comparison of Predicted and Actual Modes of Solidification in Stainless Steel Claddings**

| Sample No. | Sample Code No. | Predicted Mode SR | SMS | HR | SMH | SMW | Observed Mode |
|---|---|---|---|---|---|---|---|
| 1 | T1 | 1.51 | FA | 1.40 | AF | — | AF/FA |
| 2 | T2 | 1.70 | FA | 1.55 | FA | FA | FA |
| 3 | T3 | 1.69 | FA | 1.55 | FA | FA | FA |

SR = Ratio of $Cr_{equ}/Ni_{equ}$ based on Schaeffler equivalents.
HR = Ratio of $Cr_{equ}/Ni_{equ}$ based on Hammer and Svensson equivalents.
SMS = Predicted solidification mode based on SR.
SMH = Predicted solidification mode based on HR.
SMW = Predicted solidification mode from WRC-1992 constitutional diagram.
AF = Austenitic-ferritic mode of solidification.
FA = Ferritic-austenitic mode of solidification.

#### Evaluation of Ductility and Corrosion Resistance

Three-side bend test specimens prepared from a single layer cladded plate were bent easily through 180 deg, indicating good ductility in the cladding. From single-loop EPR curves shown in Figs. 16 and 17, it is evident that no definite reactivation peak occurred. This signals that the claddings were entirely free of sensitization and had good resistance to ICC. This may be attributed to the lower carbon content of the cladding and compositions of the claddings met the required standard composition. It is apparent from Figs. 18 and 19 that both double-loop EPR curves show no peak current in the reverse scan. This indicates that all claddings were having good resistance to ICC.

## Conclusions

The following conclusions are drawn from the investigations reported in this paper:

1) Either high voltage and high welding speed or low voltage and low welding speed produced low dilution.

2) Compositional requirements of ER316L can be met in the 316L multilayer cladding and the carbon content of second and third layers was less than 0.03%.

3) Transition or intermediate mixed zones existing in stainless steel cladding have an intermediate composition between base metal and weld metal compositions, which result in a hard martensitic structure.

4) Ferrite content in the multilayer cladding is more than that in single layer cladding.

5) Color metallographic technique is an effective tool to reveal primary as well as secondary microstructure in stainless steel cladding.

6) Optical metallography revealed that in the as-welded condition the microstructural constituents of the HAZ, fusion boundary zone, and claddings surfaced at a low dilution condition were bainite and ferrite, martensite, and austenite plus ferrite, respectively.

7) The solidification modes assessed on the basis of microstructures were well in agreement with the predicted modes of solidification from the ratios of equivalents based on Schaeffler, and Hammer and Svensson equivalents.

8) Cladding surfaced at low dilution conditions possessed good ductility and resistance to intergranular corrosion.

*References*


1. Stewart, J. P. 1981. *The Welder's Handbook*. pp. 163–219, Virginia, Restor Publ. Co., Inc.

2. Wylie, R. D., McDonald, J. Jr., and Lowenberg, A. L. 1965. Weld deposited cladding of pressure vessels. *British Welding Journal* 12(8): 378–393.

3. Nakano, S., *et al.* 1982. MAGLAY-an electroslag technique for overlay welding. *Metal Construction*, pp. 610–613.

4. Prasad Rao, K., and Prasannakumar. 1981. Investigations into characteristics and corrosion behavior of strip cladding. *Proc. National Welding Seminar*, IIW, India, pp. 29–37.

5. Gautam, D. K., and Breazu N. 1988. Some aspects of MIG stainless steel cladding. *Proc. Int. Conf. on Welding Tech.* Univ. of Roorkee, India, pp. I-145-I-151.

6. McGlone, J. C. 1982. Weld bead geometry prediction—a review. *Metal Construction* 14: 378–384.

7. Harris, P., and Smith, B. L. 1983. Factorial techniques for weld quality prediction. *Metal Construction*. 15: 661–666.

8. Raveendra, J., and Parmar, R. S. 1987. Mathematical models to predict weld bead geometry for flux cored arc welding. *Metal Construction* 19: 31R–35R.

9. Murugan, N., and Parmar, R. S. 1993. Effect of submerged arc process variables on dilution and bead geometry in single wire surfacing. *Journal of Materials Processing Technology* 37: 767–780.

10. Murugan, N., and Parmar, R. S. 1993. Mathematical models for prediction of dilution and bead geometry in single wire submerged arc surfacing. *Proc. of National Welding Seminar*, IIW, Bhilai, pp. 44(a)–44(c).

11. American Society for Metals. 1983. *Metals Handbook*, 9th Ed., Vol. 6., Materials Park, Ohio, p. 804.

12. Lancaster, J. F. 1987. *The Metallurgy of Welding*, 4th Ed., Allen and Unwin, London.

13. Beraha, E., and Shpigler, B. 1977.

*Color Metallography*. American Society for Metals, Metals Park, Ohio.

14. Gunter Petzow. 1978. *Metallographic Etching.*. ASM International, Metals Park, Ohio.

15. Long, C. J., and Delong, W. T. 1973. The ferrite content of austentitic stainless steel weld metal. *Welding Journal* 52(7):281-s to 297-s.

16. Castro, R., and Cadenet, J. J. de. 1974. *Welding Metallurgy of Stainless and Heat-Resisting Steels*, London, Cambridge Univ. Press, p. 90.

17 Olson, D. L 1985. Prediction of austenite weld metal microstructure and properties. *Welding Journal* 64(10):281-s to 295-s.

18. Erich Folkhard. 1984. *Welding Metallurgy of Stainless Steels*, New York, Spinger-Verlag.

19. Kujanpaa, V. P. 1985. Effects of steel type and impurities in solidification cracking of austenitic stainless steel welds. *Metal Construction* 17: 40R–46R.

20. Majidi, A. P., and Streicher, M. A. 1984. Potentiodynamic reactivation method for detecting sensitization in AISI 304 and 304L stainless steels. *Corrosion* 40: 393–408.

21. Klueh, R. L., and King, J. F. 1982. Austenitic stainless steel-ferritic steel weld joint failures. *Welding Journal* 61(9): 302-s to 311-s.

22. Kravstov, T. G., *et al.* 1988. Structure of the metal in the fusion zone in depositing austenitic steel on pearlitic steel. *Avomaticheskava Svarka* 41(2): 10–13.

23. Lundin, C. D., Delong, W. T., and Spond, D. F. 1975. Ferrite fissuring relationship in austenitic stainless steel weld metals. *Welding Journal* 54: 241-s to 246-s.

24. Smith, D. V. 1988. A practical approach to ferrite in stainless steel weld metal. *Welding Journal* 67(6): 57–60.

25. Kotecki, D. J., and Siewert, T. A. 1992. WRC-1992 constitution diagram for stainless steel weld metals: A modification of the WRC-1988 diagram. *Welding Journal* 71 (5): 171-s to 178-s.

26. Thier, H., Killing, R., and Killing, U. 1984. Solidification modes of weldments in corrosion resistant steels – how to make them visible. *Metal Construction* 16(3): 127–130.

27. Thomas Doody. 1992. Intermediate mixed zones in dissimilar metal welds for sour service. *Welding Journal* 71(3): 55–60.

28. Kujanpaa, V. P., *et al.* 1980. Solidification cracking estimation of the susceptibility of austenitic and austenitic-ferritic stainless steel welds. *Metal Construction* (6): 282–285.

29. Suutala, N. 1983. Effect of solidification conditions on the solidification mode in austinitic stainless steels. *Metallurgical Transactions* 14A (2): 191–197.

## PAPERS SOUGHT FOR INTERNATIONAL LASER MEETING

Abstracts on materials processing, medicine and medical devices due April 30.

The Laser Institute of America, a nonprofit society devoted to fostering education and knowledge about lasers, laser applications and laser safety, is seeking submissions for presentation at the 16th International Congress on Applications of Lasers and Electro-Optics (ICALEO'97), which will be held November 17–20 in San Diego, Calif.

Organizers will consider requests from authors who wish to submit papers for presentation, as well as proposals for a series of hands-on educational short courses related to laser applications in manufacturing. Abstracts should clearly describe original work of recent origin or contain previously unpublished results of application research, development or other implementation. The submission deadline is April 30.

ICALEO'97 is an international forum for the exchange of technical information between those who use lasers or electro-optic technologies in industrial, government and academic settings and the scientists, engineers and technicians engaged in developing these new technologies and applications. ICALEO'97 will include technical papers, poster sessions, panel discussions, short courses and a vendor day.

Papers are sought on materials processing applications in aerospace, welding, electronics, microprocessing, rapid prototyping, surface modifications, cutting and drilling, process modeling and control, laser safety, laser systems and applications, and new developments in laser equipment and technology. Authors are asked to secure company and/or governmental agency clearance to present and publish as early as possible. Commitments for travel and accommodation funding through sponsoring organizations should be obtained prior to submitting abstracts.

Areas of special interest in the medicine and medical devices field are dermatology (skin resurfacing, hair removal, etc.), drug delivery, TMLR, laser-assisted cellular surgery, stents, catheters, sensors, implantable devices, new materials, micro-fabrications, micro-molding, cutting, drilling and welding, rapid prototyping and wire stripping.

If you have any questions about the conference, please do not hesitate to call conference coordinator Daryl Flynn at the Laser Institute of America, 12424 Research Parkway, Suite 125, Orlando, FL 32826. Telephone (407) 380-1553 or (800) 345-2737, Fax (407) 380-5588.